

Nonlinear dynamo action in a precessing cylindrical containerC. Nore,¹ J. Léorat,² J.-L. Guermond,^{1,3} and F. Luddens^{1,3,*}¹*Laboratoire d'Informatique pour la Mécanique et les Sciences de l'Ingénieur, CNRS UPR 3251, BP 133, F-91403 Orsay cedex, France, Université Paris-Sud 11, 91405 Orsay cedex, France, and Institut Universitaire de France, 103 bd Saint Michel, 75005 Paris, France*²*Luth, Observatoire de Paris-Meudon, place Janssen, F-92195-Meudon, France*³*Department of Mathematics, Texas A&M University, 3368 TAMU, College Station, Texas 77843-3368, USA*

(Received 10 February 2011; revised manuscript received 13 May 2011; published 28 July 2011)

It is numerically demonstrated by means of a magnetohydrodynamics code that precession can trigger the dynamo effect in a cylindrical container. When the Reynolds number, based on the radius of the cylinder and its angular velocity, increases, the flow, which is initially centrosymmetric, loses its stability and bifurcates to a quasiperiodic motion. This unsteady and asymmetric flow is shown to be capable of sustaining dynamo action in the linear and nonlinear regimes. The magnetic field thus generated is unsteady and quadrupolar. These numerical evidences of dynamo action in a precessing cylindrical container may be useful for an experiment now planned at the Dresden sodium facility for dynamo and thermohydraulic studies in Germany.

DOI: [10.1103/PhysRevE.84.016317](https://doi.org/10.1103/PhysRevE.84.016317)

PACS number(s): 47.65.-d, 52.30.Cv, 52.65.Kj, 91.25.Cw

I. INTRODUCTION

The interest of astronomers and physicists for the dynamo action finds its origins in the quest for a reasonable explanation for the source of terrestrial and solar magnetism. Dynamo action is obtained when the conversion rate of kinetic energy in magnetic energy in the Earth's liquid core is larger than the ohmic dissipation. This phenomenon is turbulent, and reproducing it either numerically or experimentally constitutes an enormous challenge.

For a long time the analysis of the dynamo action has been restricted to kinematic dynamo theories that postulate that the velocity field is known *a priori*. For instance, the so-called mean-field theory consists of assuming that the velocity and magnetic length scales are well separated and the magnetic Reynolds number is small. Although the mean-field theory is widely used, its validity in the range of large magnetic Reynolds number is questionable [1,2].

Some models, like the so-called alpha-quenching model, include some sort of nonlinear retroaction of the fluid flow on the magnetic field through a modeling of the velocity perturbations as a function of the local magnetic field. These models do give saturated nonlinear dynamics, but, again, the theoretical foundations of these approaches are questionable.

One can imagine that, as the number-crunching capacity of computers is ever growing, some of the shortcomings of the above phenomenological theories and models can be overcome by direct numerical simulation (DNS) of the magnetohydrodynamics (MHD) equations. Although the main advantage of the direct numerical simulation approach is that the nonlinear coupling between the Navier-Stokes equations and the induction equation is represented exactly, some level of modeling of the boundary conditions and forcing is still required by DNS. For instance, the question of the nature of the forcing that needs to be applied to the MHD system so the resulting dynamo has experimental or astronomical significance needs to be somewhat modelled. The purpose of

the remainder of this introduction is to briefly review this issue, and the objective of this paper is to show that precession is an efficient forcing that can be used for experimental purposes and does not require any modeling.

DNS of the dynamo action is very demanding computationally since obtaining statistically stationary solutions requires very long integration times. Two types of DNS are performed in practice to address this problem. If one is interested in the dynamics of length scales that are significantly smaller than those of the forcing term (i.e., the source of energy in the system), one can use periodic conditions together with the very efficient arsenal of Fourier/spectral techniques. This is the choice usually made for the study of turbulent dynamos. If, on the other hand, one is interested in the dynamics of scales that are close to the characteristic scales of the forcing term, one must represent the boundary conditions more accurately and thus use numerical methods that are not yet as efficient as spectral methods and thus cannot reach very high Reynolds numbers. This type of choice is made when one wants to study large-scale dynamos. Forcing by precession, which is the object of this paper, can be put in this category. Let us now review the various types of nonlinear dynamos known so far to better appreciate the qualities of precession forcing.

In the standard framework of homogeneous MHD turbulence, the mechanical power injected in the system is modelled by a large-scale forcing term that can be either time independent or random with zero or finite correlation time. The purpose of the turbulent dynamos thus generated is to study the dynamics of the energy transfers between scales and between the velocity and the magnetic fields [3–6]. It is sufficient to use periodic boundary conditions to achieve this program. Let us emphasize, though, that this type of simulation is not yet capable of drawing reasonable conclusions concerning the terrestrial magnetism, since the magnetic Prandtl numbers explored so far, P_m , are larger than 0.01, whereas the terrestrial magnetic Prandtl number is very small, $P_m \approx 10^{-5}$.

Contrary to turbulent dynamos, it is critical to impose realistic boundary conditions in large-scale dynamos. Although natural and experimental dynamos have simple geometries in general, modeling their forcing for numerical purposes

*nore@limsi.fr

is nontrivial. For instance, thermal convection is known to be a source of stellar dynamos, and it is also suspected to be one of the possible sources of the geodynamo [7], but enforcing a realistic boundary condition to control the thermal convection is a particularly tricky question for the geodynamo. It is now recognized that various numerical scenarios can be obtained depending on the nature of the boundary condition that is imposed at the boundary of the iron core; see, for instance, Refs. [8–10]. The situation is similar for experimental dynamos driven either by rotors or pumps [11–13]. In this case as well, forcing is usually modelled by inserting *ad hoc* forces in the momentum equation; see, for instance, Refs. [14–16].

Contrary to the above examples, precession has the rare quality of generating a flow dynamics free of modeling, since exact boundary conditions are imposed in this case. The boundary conditions prescribe the action of the container walls on the flow and thus create a realistic forcing at the largest scale available. Simulating numerically precession-driven rotating flows is useful for experimental fluid dynamos and opens perspectives for real astrophysical dynamos [17,18]. To the best of our knowledge, only two precession-driven dynamos have been successfully simulated so far. Tilgner [19,20] has first proved the capability of precession to drive the dynamo effect in a spherical shell. However, due to the symmetry properties of the sphere, the precessing flow thus obtained is driven by viscosity, which makes it difficult to be used in experimental and astrophysical applications at large kinetic Reynolds numbers. Wu and Roberts [21] have obtained the dynamo effect in a precessing spheroid using a flow obtained as a stress free fluctuation of an analytical Poincaré solution. The objective of the paper is to show that dynamo action can also be achieved in a precessing cylinder. The precession forcing in a cylinder is large scale, i.e., comes from the walls and is not purely viscous. Although the spheroidal geometry is more relevant in an astrophysical context, the cylindrical geometry is more suitable for experimental purposes. A first attempt to realize an experimental turbulent homogeneous dynamo in a precessing cylindrical container is reported in Ref. [22]. A new experiment using a cylindrical vessel is now planned in the large-scale MHD facility DRESDYN currently being built at Helmholtz-Zentrum Dresden-Rossendorf in Germany. The action of precession will be tested there, among other things (F. Stefani [23]).

The objective of the present article is to report numerical evidence supporting the idea that precession is indeed a potent mechanism to drive dynamo action in cylindrical containers. The paper is organized as follows. The formulation of the problem is described in Sec. II. We present in Sec. III the hydrodynamical regimes that are obtained at different Reynolds numbers, focusing on the two largest ones. Section IV explores the dynamo action in linear and nonlinear regimes. The role of symmetries is also investigated in this section. Section V is devoted to a discussion of the results.

II. FORMULATION OF THE PROBLEM

The conducting domain considered in this article is a cylindrical vessel \mathcal{C} of radius R and length L . The vessel contains a conducting fluid and is embedded in vacuum. The solid walls of the vessel are assumed to be so thin that their

influence is henceforth neglected. The container rotates about its axis of symmetry with angular velocity $\Omega_r \mathbf{e}_z$ and is assumed to precess about a second axis spanned by the unit vector \mathbf{e}_p forming an angle α with \mathbf{e}_z , ($0 < \alpha < \pi$). The angular velocity of the precession is $\Omega_p \mathbf{e}_p$. A cylindrical coordinate system about the axis of the cylinder is defined as follows: the origin of the coordinate system is the center of mass of the cylinder, say O ; the Oz axis is the line passing through O and parallel to \mathbf{e}_z ; the origin of the angular coordinate θ ($0 \leq \theta \leq 2\pi$) is the half-plane passing through O , spanned by \mathbf{e}_z and \mathbf{e}_p , and containing the vector $\Omega_p \mathbf{e}_p$. The third coordinate, denoted r , is the distance to the Oz axis.

We denote by $\mathcal{L} = R$ and $\mathcal{U} = R\Omega_r$ the reference length and velocity scales, respectively. The fluid density, ρ , is assumed to be constant and the reference pressure scale is $\mathcal{P} := \rho\mathcal{U}^2$. The magnetic permeability is uniform throughout the entire space, μ_0 , and the electric conductivity of the conducting fluid is constant, σ_0 . The quantities μ_0 and σ_0 are used as reference magnetic permeability and electric conductivity, respectively. The reference scale for the magnetic field is chosen so the reference Alfvén speed is 1, i.e., $\mathcal{H} := \mathcal{U}\sqrt{\rho/\mu_0}$. We are left with five nondimensional parameters: one geometrical parameter L/R (aspect ratio); two forcing parameters α (precession angle) and $\varepsilon = \Omega_p/\Omega_r$ (precession rate); and two fluid parameters, namely the Ekman number $E = \nu/R^2\Omega_r$ (where ν is the kinematic viscosity) and the magnetic Prandtl number $P_m = \nu\mu_0\sigma_0$. We finally define the kinetic Reynolds number $R_e = 1/E$ and the magnetic Reynolds number $R_m = P_m R_e$.

The nondimensional set of equations that we consider is written as follows in the precessing frame of reference:

$$\begin{aligned} \partial_t \mathbf{u} + (\mathbf{u} \cdot \nabla) \mathbf{u} + 2\varepsilon \mathbf{e}_p \times \mathbf{u} + \nabla p &= \frac{1}{R_e} \Delta \mathbf{u} + \mathbf{f}, \\ \nabla \cdot \mathbf{u} &= 0, \\ \partial_t \mathbf{h} - \nabla \times (\mathbf{u} \times \mathbf{h}) &= \frac{1}{R_m} \Delta \mathbf{h}, \\ \nabla \cdot \mathbf{h} &= 0, \end{aligned}$$

where \mathbf{u} , p , and \mathbf{h} are the velocity field, the pressure, and the magnetic field, respectively. In the following we consider three different settings to solve these equations: (i) The incompressible Navier-Stokes setting; (ii) the Maxwell or kinematic dynamo setting; and (iii) the nonlinear MHD setting. In the Navier-Stokes setting the source term \mathbf{f} is set to zero and \mathbf{h} is not computed. In the Maxwell setting, only the induction equation is solved, assuming that the velocity field \mathbf{u} is given. In the MHD setting the full set of equations is solved and the source term \mathbf{f} is the Lorentz force per unit mass, $\mathbf{f} := (\nabla \times \mathbf{h}) \times \mathbf{h}$. The no-slip boundary condition on the velocity field is written as follows in the precessing frame of reference: $\mathbf{u} = \mathbf{e}_\theta$ at $r = 1$ and $\mathbf{u} = r\mathbf{e}_\theta$ at $z = \pm 1$. The magnetic field is represented as the gradient of a scalar potential, $\nabla\phi$, in the vacuum. The magnetic boundary transmission conditions enforce that the magnetic field is continuous across the walls of the vessel, say Σ , i.e., $\mathbf{h}|_\Sigma = \nabla\phi|_\Sigma$.

The above equations are solved numerically by means of a code that is specialized to axisymmetric domains and has been presented in detail in Refs. [24,25]. The code is called spectral/finite elements for Maxwell and Navier-Stokes

equations (SFEMaNS). It is a hybrid algorithm that uses finite element representations in the meridian section of the axisymmetric domain and Fourier representations in the azimuthal direction. The magnetic field is represented as a vector field in the conducting region and as the gradient of a scalar potential in the insulating region. SFEMaNS can account for discontinuous distributions of electric conductivity and magnetic permeability, and all the required continuity conditions across the interfaces are enforced using an interior penalty technique. The solution technique is parallel and parallelization is done with respect to the Fourier modes.

The typical spatial resolution in the meridional plane of the conducting domain is $\Delta x = 1/160$. The grid is nonuniform in the vacuum with $\Delta x = 1/160$ close to the cylindrical vessel and $\Delta x = 1$ at the outer boundary of the numerical domain, which is a sphere of a radius 10 times larger than that of the cylinder. We take 24 or 32 Fourier modes ($m = 0, \dots, 23$ or $m = 0, \dots, 31$) for Navier-Stokes runs and 64 Fourier modes ($m = 0, \dots, 63$) for MHD runs. The typical time step is $\Delta t = 0.001$. A typical MHD run requires about 1000 cumulated CPU hours per rotation ($t = 2\pi$) on 64 processors on an IBM-SP6.

III. HYDRODYNAMICAL REGIME

Let us now briefly recall what is observed in a typical precessing fluid experiment starting with the fluid at rest (see, e.g., Refs [26–28]). The vessel is first set in rotation without precession. The fluid motion is then governed by the formation of a viscous Ekman boundary layer during the acceleration ramp. The resulting flow is a stable solid rotation independently of the strength of the acceleration phase. Once precession is applied, the Coriolis force generates an axial motion of the flow driven by the Fourier mode $m = 1$. When R_e is large enough, the flow undergoes a transition from laminar to turbulent even for small precession rates and small angles [27]. The range $\varepsilon \in [0.1, 0.15]$ was shown in Ref. [26] to maximize the axial energy in a cylinder of aspect ratio 2 in the range $R_e \in [500, 5000]$ when $\alpha = \pi/2$. Although a parametric study varying the aspect ratio, the precession angle and the precession rate is interesting per se, due to limited numerical resource we are going to reduce the dimensionality of the parametric space to one aspect ratio, $L/R = 2$, one precession angle, $\alpha = \pi/2$, one precession rate, $\varepsilon = 0.15$, four values of $R_m \in \{600, 800, 1200, 2400\}$, and a larger range of $R_e \in [400, 1200]$.

A. Axial and total kinetic energies

We start our investigations with a Navier-Stokes run at $R_e = 1000$. The initial velocity field is the solid rotation in the precessing frame: $\mathbf{u}_0 = \mathbf{e}_z \times \mathbf{r}$. The onset of the axial circulation induced by precession is monitored by recording the time evolution of the normalized total kinetic energy $K(t) = \frac{1}{2} \int_C \mathbf{u}^2(\mathbf{r}, t) d\mathbf{r} / K_0$ and normalized axial kinetic energy $K_z(t) = \frac{1}{2} \int_C u_z^2(\mathbf{r}, t) d\mathbf{r} / K_0$, where $K_0 = \frac{1}{2} \int_C \mathbf{u}_0^2 d\mathbf{r}$ is the kinetic energy of the initial motion. The time evolution of $K(t)$ and $K_z(t)$ for $t \in [0, 297]$ is reported in Fig. 1. The time $t = 297$ corresponds to 47.3 rotation periods. After a transient that lasts five rotation periods and peaks at two rotation periods, the axial kinetic energy oscillates around a plateau value

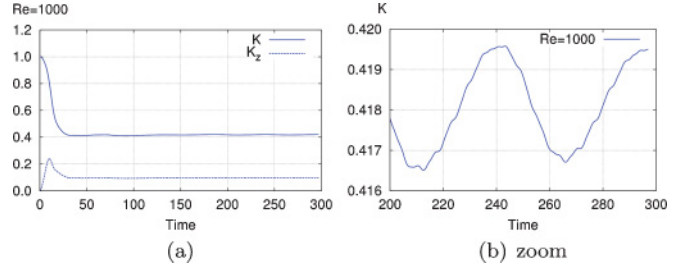


FIG. 1. (Color online) Time evolution of the total kinetic energy K and axial kinetic energy K_z at $R_e = 1000$ and zoom of K .

$K_z \approx 0.1$. Meanwhile, the total kinetic energy decreases and oscillates around a plateau value $K \approx 0.418$ also after five rotation periods. These values are in very good agreement with those reported in Fig. 1 of [26]. The time evolution of the total kinetic energy shown in Fig. 1(b) presents doubly periodic oscillations with one long period of about nine rotation periods and one small period of about one rotation period.

To enrich the dynamics of the system we have restarted the computation at $t = 72$ (i.e., 11.5 rotation periods) and increased the Reynolds number to $R_e = 1200$. The time evolution of $K(t)$ and $K_z(t)$ at $R_e = 1200$ for $t \in [72, 342]$ and at $R_e = 1000$ for $t \in [0, 275]$ is reported in Fig. 2. At saturation, the time evolution of the total kinetic energy exhibits doubly periodic oscillations as can be seen in Fig. 2(c) for $R_e = 1200$. The short period oscillations correspond to energy exchanges between the north and south halves of the container, with a period of about two rotation periods. The energy exchange mechanism is visible in Fig. 2(d) where we have reported the time evolution of the kinetic energy of the north and south halves of the cylinder for $t \in [312, 342]$. Similar oscillations between north and south hemispheres have been reported to occur in a spheroidal cavity in Ref. [21].

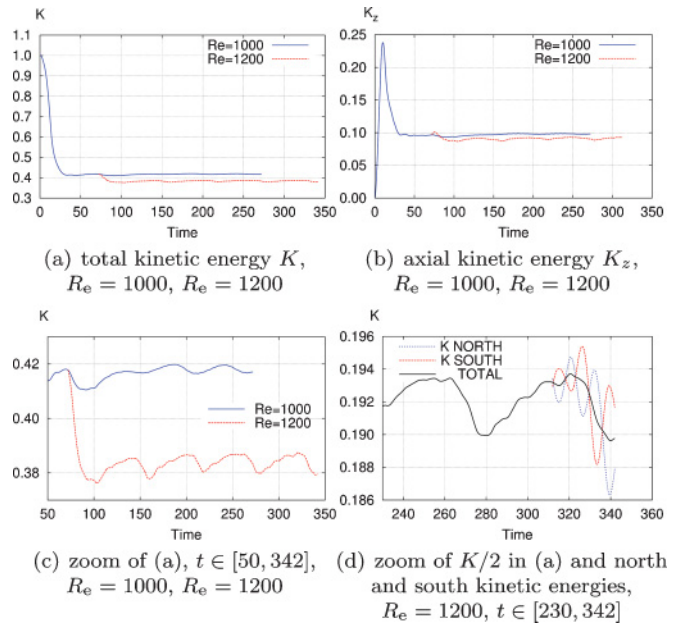


FIG. 2. (Color online) Time evolution of the total kinetic energy K , axial kinetic energy K_z , and total north and south kinetic energies as indicated.

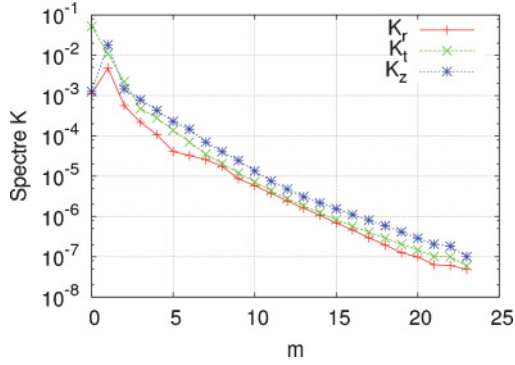


FIG. 3. (Color online) Time averaged spectra of the three components of the velocity field as a function of the azimuthal mode $m = 0, \dots, 23$ at $Re = 1200$.

More can be learned by examining spectra instead of integrated quantities like the total kinetic energy K . We show, for instance, in Fig. 3 the time-averaged azimuthal spectra of the three velocity components at $Re = 1200$. More precisely, the quantities shown are $K_i(m) := \frac{1}{T} \int_0^T [\int \frac{1}{2} |\hat{u}_i(r, m, z, t)|^2 dr dz] dt$, where $\hat{u}_i(r, m, z, t)$ is the m th Fourier component of the velocity component $u_i(r, \theta, z, t)$, $i \in \{r, \theta, z\}$. The maximum at $m = 0$ of the azimuthal energy spectrum $K_\theta(m)$ corresponds to the large-scale forcing induced by the rotating walls. The maximum at $m = 1$ of $K_z(m)$ corresponds to the Coriolis acceleration. The radial energy spectrum $K_r(m)$ presents also a maximum at $m = 1$. The three velocity components show parallel spectra at large wave numbers as a consequence of nonlinear coupling and transfer toward the dissipation scale.

In the MHD runs reported below, we have used $Re = 1200$ since the corresponding hydrodynamical regime has broken the centrosymmetry and thus seems favourable for dynamo action.

B. Transition at low kinetic Reynolds numbers

Before investigating the dynamo regime we want to explore the dynamics of the centro-symmetry breaking in the Navier-Stokes regime as the Reynolds number increases.

Figure 4 displays the total kinetic energy in the range $Re \in [400, 1200]$. Note that K is a decreasing function of Re in this range (see the discussion in Sec. V). At low Reynolds

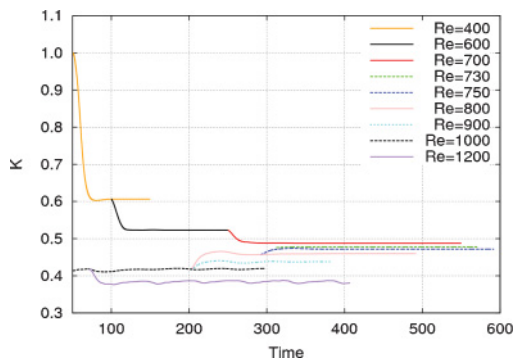


FIG. 4. (Color online) Time evolution of the total kinetic energy K for different Reynolds numbers $Re \in [400, 1200]$.

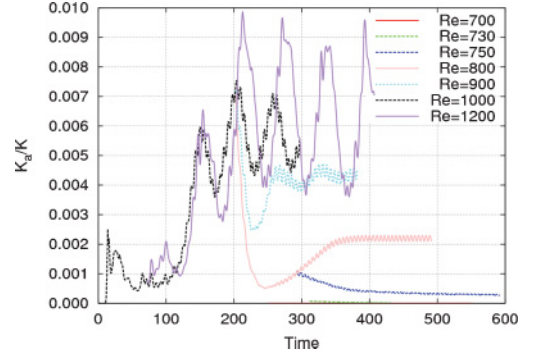


FIG. 5. (Color online) Time evolution of the asymmetry ratio r_a for different Reynolds numbers $Re \in [700, 1200]$.

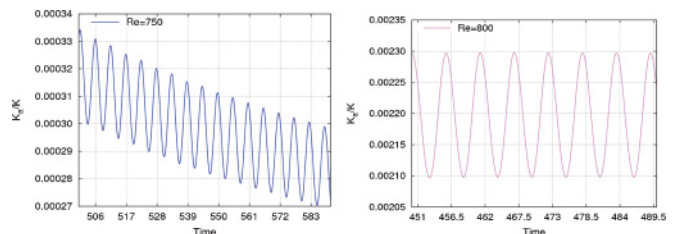
numbers, e.g., at $Re = 700$, the velocity field is steady and centrosymmetric, meaning that $\mathbf{u}(\mathbf{r}, t) = \mathbf{u}(\mathbf{r}) = -\mathbf{u}(-\mathbf{r})$.

At larger Reynolds numbers, the loss of centrosymmetry of the velocity field can be monitored by inspecting its symmetric and antisymmetric components: $\mathbf{u}_s(\mathbf{r}, t) = \frac{1}{2}[\mathbf{u}(\mathbf{r}, t) + \mathbf{u}(-\mathbf{r}, t)]$ and $\mathbf{u}_a(\mathbf{r}, t) = \frac{1}{2}[\mathbf{u}(\mathbf{r}, t) - \mathbf{u}(-\mathbf{r}, t)]$. In the Navier-Stokes simulations reported below, we monitor the loss of centrosymmetry by tracking the time evolution of the asymmetric kinetic energy $K_a(t) = \frac{1}{2} \int_C \mathbf{u}_a^2(\mathbf{r}, t) d\mathbf{r} / K_0$ and the asymmetry ratio $r_a(t) = K_a(t) / K(t)$. These computations have been done on centrosymmetric grids, but centrosymmetry has not been otherwise enforced. Figure 5 shows that the asymmetry ratio decreases as time grows at $Re = 750$ [see also the enlarged view in Fig. 6(a)] and is always below 10^{-6} at $Re = 700$ and 730 . At $Re = 800$, the velocity field is unsteady and asymmetric; the asymmetry ratio $r_a(t)$ oscillates around the asymptotic value 0.0022 as shown in Fig. 6(b). At $Re = 900$ and above, the flow is clearly asymmetric and the time evolution of the total kinetic energy is quasiperiodic with a short period of about one rotation period and a long period of about nine rotation periods; see Fig. 4.

IV. DYNAMO ACTION

A. Linear regime

We now solve the full MHD system using as initial velocity field the velocity computed at $t = 192$ during the Navier-Stokes run at $Re = 1200$. The initial magnetic field and the boundary conditions on the scalar potential are defined as follows in order to trigger efficiently the dynamo instability. The zero Dirichlet boundary condition that was

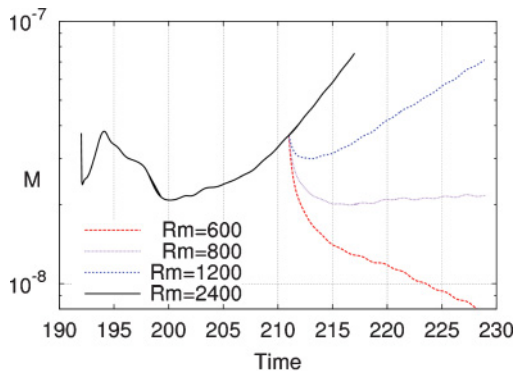


(a) zoom of r_a at $Re = 750$ (b) zoom of r_a at $Re = 800$

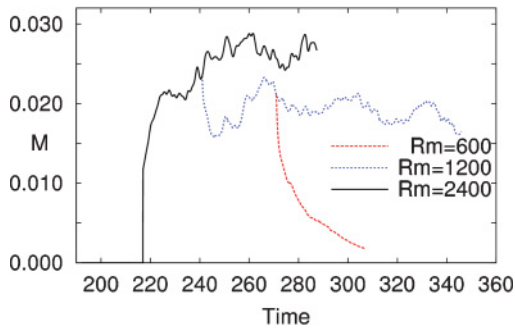
FIG. 6. (Color online) Time evolution of the asymmetry ratio r_a at $Re = 750$ and $Re = 800$ to show the short period of oscillations.

imposed on the scalar potential ϕ on the outer sphere is replaced by $\hat{\phi}_0 = 0.05zf(t)$ for $m = 0$ and $\hat{\phi}_1 = 0.05rf(t)$ for $m = 1$, where $f(t) = \frac{\tau_a^3}{1+\tau_a^3}(1 - \frac{\tau_e^4}{1+\tau_e^4})$ with $\tau_a = \frac{t}{0.4}$ and $\tau_e = \frac{t}{2}$, and the amplitude of each Fourier mode of the initial magnetic field components is set to 10^{-5} for $m \geq 2$. It has been verified in Ref. [29] that imposing vanishing Dirichlet boundary conditions on ϕ on a sphere of radius 10 times larger than the typical scale of the conducting region gives results that are very close to those obtained by imposing Neumann or Robin boundary conditions.

Various MHD runs are done at $R_e = 1200$ for different values of the magnetic Prandtl number. The onset of dynamo action is monitored by recording the time evolution of the magnetic energy in the conducting fluid, $M(t) = \frac{1}{2} \int_C \mathbf{h}^2(\mathbf{r}, t) d\mathbf{r} / K_0$. Linear dynamo action occurs when $M(t)$ is an increasing function of time for large times. The time evolution of M for $P_m \in \{2, 1, \frac{2}{3}, \frac{1}{2}\}$ is shown in Fig. 7(a). The runs at $P_m \in \{1, \frac{2}{3}, \frac{1}{2}\}$ are done by using the velocity and magnetic fields obtained from the run $P_m = 2$ at $t = 211$ as initial velocity and magnetic fields. The flow is observed to be above the dynamo threshold at $P_m = 1$ and $P_m = \frac{2}{3}$ but is subcritical at $P_m = \frac{1}{2}$. Linear interpolation of the growth rates gives the critical magnetic Prandtl number $P_m^* \approx 0.625$ corresponding to the critical magnetic Reynolds number $R_m^* \approx 750$.



(a) linear regime



(b) nonlinear regime

FIG. 7. (Color online) Time evolution of the magnetic energy M in the conducting fluid (a) in the linear regime from $t = 192$ at $R_e = 1200$ and various R_m as indicated (in lin-log scale) and (b) in the nonlinear regime from $t = 192$ to $t = 287.5$ ($R_e = 1200$, $R_m = 2400$), from $t = 241$ to $t = 346$ ($R_e = 1200$, $R_m = 1200$), and from $t = 271$ to $t = 307$ ($R_e = 1200$, $R_m = 600$).

B. Nonlinear saturation

We now want to observe the nonlinear saturation and evaluate the impact of the magnetic Prandtl number on the nonlinear regime. To reach nonlinear saturation in reasonable CPU time, we have used as initial data for the velocity and magnetic fields the velocity and magnetic fields from the MHD run at $t = 217$ with $P_m = 2$. The velocity field has been kept unchanged but we have multiplied by 300 the amplitude of the Fourier modes $m = 0, \dots, 5$ of the magnetic field. The time evolution of the magnetic energy of this nonlinear run in the time interval $t \in [192, 287.5]$ is shown in Fig. 7(b). We observe that M grows smoothly in one turnover time (i.e., until $t \approx 222$) and begins to oscillate thereafter. The ratio M/K is observed to be of order 6×10^{-2} during the nonlinear oscillating regime. After restarting the MHD run at $t = 241$ with $P_m = 1$ and running it until $t = 346$, we observe that the dynamo is still active. After restarting the MHD run at $t = 271$ with $P_m = \frac{1}{2}$ and running it until $t = 307$, we observe that the dynamo dies in a short time, suggesting that the dynamo bifurcation is not subcritical for this set of control parameters. These nonlinear results indicate that P_m^* lies in the interval $[\frac{1}{2}, 1]$. Recall that the threshold determined in the linear regime is $P_m^* \approx 0.625$.

A snapshot of the vorticity and magnetic lines at $R_e = 1200$, $R_m = 2400$ is shown in Fig. 8. We observe a central S-shaped vortex that is deformed by the precession and reconnects at the walls through viscous boundary layers [see Fig. 8(a)]. The magnetic field lines exhibit a quadrupolar shape that is best seen in the vacuum from the top of the cylinder [see Fig. 8(b)]. These lines connect mainly to the lateral wall where the current is concentrated. The magnetic energy in the cylinder is dominated by the azimuthal modes $m = 1, 2, 3$.

C. Role of the flow symmetries

Tilgner [19] has observed that unsteadiness and breaking of the centrosymmetry of the flow facilitate dynamo action. A similar observation has been made in Ref. [21], and dynamo action is reported therein to occur when cyclic oscillations of the kinetic energy between the north and south halves of the spheroidal cavity occur. Although the loss of centrosymmetry

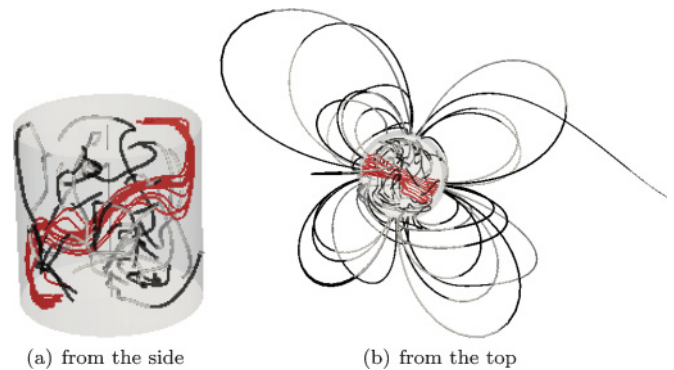


FIG. 8. (Color online) Snapshot at $t = 241$ for $R_e = 1200$, $R_m = 2400$ showing vorticity field lines (red) and magnetic field lines colored by the axial component [(gray (black) for positive (negative) H_z component)].

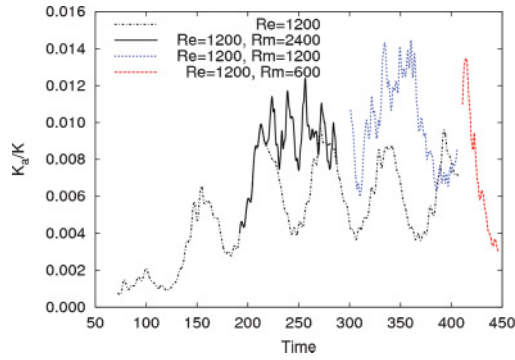


FIG. 9. (Color online) Time evolution of the asymmetry ratio r_a at $Re = 1200$ for $t \in [72, 407]$ in the Navier-Stokes setting and $Re = 1200, R_m = 2400$ for $t \in [192, 287.5]$, $Re = 1200, R_m = 1200$ for $t \in [241, 346]$, and $Re = 1200, R_m = 600$ for $t \in [271, 307]$ in the MHD setting. The curves at $Re = 1200, R_m = 1200$ and $Re = 1200, R_m = 600$ have been shifted for easy reading.

is not a necessary condition for dynamo action, we now want to test this idea in the present cylindrical setting.

The time evolution of the asymmetry ratio r_a for the Navier-Stokes run at $Re = 1200$ is shown in Fig. 9 in the time range $t \in [72, 407]$ (dotted line). The ratio r_a varies between 0.004 and 0.01 when the nonlinear regime is well established, i.e., $t \geq 220$.

In order to evaluate the impact of the dynamo on the centrosymmetry of the flow, we have started the MHD run at $t = 192$ with $P_m = 2$ (i.e., $R_m = 2400$). The time evolution of r_a in this MHD run is shown in solid line in Fig. 9. Note that the solid and dotted lines coincide since the dynamo regime is linear in the time interval $t \in [192, 217]$ and the magnetic field is too weak to have an impact on the kinetic energy ratio r_a . We have restarted the MHD run at $t = 217$ after multiplying the amplitude of the magnetic field by 300 as already mentioned. The ratio r_a (solid line) clearly departs from its Navier-Stokes value thereafter as seen in the figure. At saturation, r_a oscillates between 0.008 and 0.012; these values are slightly larger than those reported in Ref. [19] for a precessing sphere. We have restarted the MHD run again at $t = 241$ after reducing the value of P_m to 1, thereby reducing the magnetic Reynolds number to $R_m = 1200$. The asymmetry factor (dotted blue line) also departs from its Navier-Stokes value, as seen on the figure. We have finally restarted the MHD run at $t = 271$ after reducing the value of the magnetic Prandtl number to $\frac{1}{2}$. As expected, the dynamo dies and r_a decreases to 0.003 close to the hydrodynamical level. These computations show that the dynamo action reinforces the loss of centrosymmetry of the flow.

In order to assess the impact of the centrosymmetry and of the unsteadiness of the flow on the dynamo action, we have performed two Maxwell runs at $R_m = 1200$ with the following characteristics: (i) the velocity field at $Re = 1200$ is frozen at $t = 211$ and (ii) the velocity field at $Re = 1200$ is frozen at $t = 211$ but only its symmetric component is retained so the resulting velocity field is centrosymmetric. The time evolution of the magnetic energy of the MHD run and the two Maxwell runs (i) and (ii) are shown in Fig. 10. It is remarkable that, in the two considered kinematic runs, the dynamo keeps growing with a rate similar to that of the MHD run. These

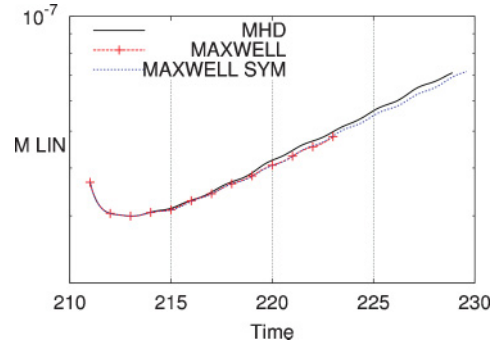


FIG. 10. (Color online) Time evolution of the magnetic energy M at $Re = 1200$ and $R_m = 1200$ for $t \in [211, 229]$ in the MHD setting (MHD), in the Maxwell setting with the velocity frozen at $t = 211$ (MAXWELL), and in the Maxwell setting with the symmetrized velocity frozen at $t = 211$ (MAXWELL SYM).

computations show that neither the temporal oscillations nor the flow asymmetry play a crucial role on the dynamo action in the precessing cylinder at $R_m = 1200$.

V. DISCUSSION

Although the range of Reynolds numbers that we have explored in our Navier-Stokes simulations is modest, it is wide enough to suggest a scaling law for the average kinetic energy, K , as a function of the Reynolds number, Re , for the precession rate, $\epsilon = 0.15$. To substantiate this claim we show in Fig. 11(b) the average K as a function of Re . The run at $Re = 2000$ has not been discussed in this paper and the points at $Re = 2500, 4000, 5000$ have been extracted from Lallemand *et al.* [26]. The log-log representation of the data suggests that in range $Re \in [400 : 5000]$ the energy scales like $K \simeq Re^{-0.4}$ [see Fig. 11(b)], which in turn suggests the following scaling law for the velocity $u \simeq Re^{-1/5} = E^{1/5}$. This scaling predicts that the average flow vanishes at large Re . This property is not paradoxical since, in an axisymmetric container with a rotation axis parallel to its symmetry axis, the azimuthal flow is driven only by viscous forces at the wall. Since in the limit of zero viscosity the rotation does not force the flow, one expects to get at the inviscid limit a static fluid in the precessing frame and a solid body motion around the precession axis in the inertial frame.

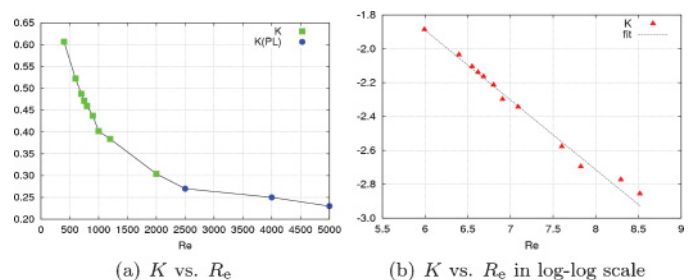


FIG. 11. (Color online) Total (time averaged) kinetic energy K in the precessing frame as a function of the Reynolds number Re : (a) the points denoted PL are from Ref. [26] and (b) log-log scale with the fit $Re^{-2/5}$.

The above scaling for the velocity reminds of the Stewartson-Roberts analysis [30] of the critical layer in a precessing sphere. Note that the range of Reynolds numbers explored here spans one decade only and the values are not large enough to reach an asymptotic regime. We mention this scaling as a possible venue for future theoretical investigations.

Forty years after the promising experiments with liquid sodium by Gans [22], we have numerically demonstrated that dynamo action can occur in a precessing cylindrical tank. The bifurcations through symmetry breaking and cyclic time dependence are similar to those already observed in dynamo flows in spherical or spheroidal precession-driven cavities. There is, however, a large gap between the control parameters used in the present simulations and those achieved in experimental setups and planetary dynamos, where $E = 1/R_e$ and P_m are many orders of magnitude smaller. Following this evidence for dynamo action, it seems that the following two directions need to be thoroughly investigated: (i) the study of parity breaking and unsteadiness through variations of the forcing parameters (precession angle and rate) and (ii) the search for a scaling law for the critical magnetic Reynolds number as a function of the hydrodynamic Reynolds number. Such a relation has been proposed by Tilgner in a precessing sphere [19], who argues that it is the asymmetric part of the flow that plays a key role in the dynamo. The research program (ii) will be time-consuming as it will necessitate large-scale computations to explore a

wide range of Reynolds numbers. It will also require the development of nonlinear stabilization techniques to simulate small scale viscous dissipation. We are currently working on a second level of parallelization of the code: In addition to the parallelization with respect to the azimuthal modes that is already implemented, we are implementing a domain decomposition technique based on PETSc [31] to solve the two-dimensional problems in the meridional domains. This will hopefully speed up the code and will permit us to perform higher-Reynolds-number computations. The empirical scaling $K \simeq R_e^{-0.4}$ that we have observed so far needs to be confirmed on smaller Ekman numbers before being considered seriously.

A major step in the understanding of precession dynamo will hopefully be achieved in the near future with the construction of the large-scale MHD facility DRESHDYN at Helmholtz-Zentrum Dresden-Rossendorf (Germany). The cooperation between simulations and experiments will lead to a better understanding of natural dynamos, including the geodynamo.

ACKNOWLEDGMENTS

This work was performed using HPC resources from GENCI-IDRIS (Grant No. 2010-0254). We acknowledge fruitful discussions with D. Cébron, W. Herreman, P. Lallemand, P. H. Roberts, F. Stefani, and A. Tilgner.

-
- [1] H. K. Moffatt, *Magnetic Field Generation in Electrically Conducting Fluids*, Cambridge Monographs on Mechanics and Applied Mathematics (Cambridge University Press, Cambridge, UK, 1978).
 - [2] F. Krause and K.-H. Radler, *Mean-Field Magnetohydrodynamics and Dynamo Theory* (Pergamon Press, Oxford, UK, 1980).
 - [3] C. Nore, M. Brachet, H. Politano, and A. Pouquet, *Phys. Plasmas* **4**, 1 (1997).
 - [4] K. Subramanian, A. Shukurov, and N. E. L. Haugen, *MNRAS* **366**, 1437 (2006).
 - [5] A. Schekochihin, A. Iskakov, S. Cowley, J. Mc Williams, M. Proctor, and T. Yousef, *New J. Phys.* **9**, 300 (2007).
 - [6] Y. Ponty, P. D. Mininni, J.-F. Pinton, H. Politano, and A. Pouquet, *New J. Phys.* **9**, 296 (2007).
 - [7] A. Kageyama, T. Miyagoshi, and T. Sato, *Nature (London)* **454**, 1106 (2008).
 - [8] G. A. Glatzmaier and P. H. Roberts, *Nature* **377**, 203 (1995).
 - [9] W. Kuang and J. Bloxham, *J. Comput. Phys.* **153**, 51 (1999).
 - [10] P. Olson, *Nature* **389**, 337 (1997).
 - [11] A. Gailitis, O. Lielausis, S. Dement'ev, E. Platacis, and A. Cifersons, *Phys. Rev. Lett.* **84**, 4365 (2000).
 - [12] R. Stieglitz and U. Müller, *Phys. Fluids* **13**, 561 (2001).
 - [13] R. Monchaux *et al.*, *Phys. Rev. Lett.* **98**, 044502 (2007).
 - [14] R. A. Bayliss, C. B. Forest, M. D. Nornberg, E. J. Spence, and P. W. Terry, *Phys. Rev. E* **75**, 026303 (2007).
 - [15] S. Kenjereš and K. Hanjalić, *Phys. Rev. Lett.* **98**, 104501 (2007).
 - [16] C. Gissinger, S. Fauve, and E. Dormy, *Phys. Rev. Lett.* **101**, 144502 (2008).
 - [17] E. C. Bullard, *Proc. R. Soc. London A* **197**, 433 (1949).
 - [18] W. V. R. Malkus, *Science* **160**, 259 (1968).
 - [19] A. Tilgner, *Phys. Fluids* **17**, 034104 (2005).
 - [20] A. Tilgner, *Geophys. Astrophys. Fluid Dyn.* **101**, 1 (2007).
 - [21] C.-C. Wu and P. Roberts, *Geophys. Astrophys. Fluid Dyn.* **103**, 467 (2009).
 - [22] R. F. Gans, *J. Fluid Mech.* **45**, 111 (1970).
 - [23] F. Stefani (personal communication).
 - [24] J.-L. Guermond, R. Laguerre, J. Léorat, and C. Nore, *J. Comput. Phys.* **228**, 2739 (2009).
 - [25] A. Giesecke, C. Nore, F. Stefani, G. Gerbeth, J. Léorat, F. Luddens, and J.-L. Guermond, *Geophys. Astrophys. Fluid Dyn.* **104**, 505 (2010).
 - [26] J. Léorat, P. Lallemand, J.-L. Guermond, and F. Plunian, in *Dynamo and dynamics, a Mathematical challenge*, Vol. 26 of NATO Science Series, II Mathematics, Physics and Chemistry, edited by P. Chossat, D. Armbruster, and I. Oprea (Kluwer, Dordrecht, 2001), pp. 25–33.
 - [27] R. Lagrange, C. Eloy, F. Nadal, and P. Meunier, *Phys. Fluids* **20**, 081701 (2008).
 - [28] T. Lehner, W. Mouhali, J. Léorat, and A. Mahalov, *Geophys. Astrophys. Fluid Dyn.* **104**, 369 (2010).
 - [29] J.-L. Guermond, R. Laguerre, J. Léorat, and C. Nore, *J. Comput. Phys.* **221**, 349 (2007).
 - [30] K. Stewartson and P. H. Roberts, *J. Fluid Mech.* **17**, 1 (1963).
 - [31] S. Balay, J. Brown, K. Buschelman, W. D. Gropp, D. Kaushik, M. G. Knepley, L. Curfman McInnes, B. F. Smith, and H. Zhang, PETSc Web page, 2011 [<http://www.mcs.anl.gov/petsc>].